

Explaining the MiniBooNE Excess Through a Mixed Model of Oscillation and Decay

S. Vergani,^{1,*} N.W. Kamp,^{2,†} A. Diaz,^{2,‡} C.A. Argüelles,^{3,§}
 J.M. Conrad,^{2,¶} M.H. Shaevitz,^{4,**} and M.A. Uchida^{1,††}

¹*University of Cambridge, Cambridge CB3 0HE, United Kingdom*

²*Dept. of Physics, Massachusetts Institute of Technology, Cambridge, MA 02139, USA*

³*Dept. of Physics, Harvard University, Cambridge, MA 02138, USA*

⁴*Dept. of Physics, Columbia University, New York, NY, 10027, USA*

(Dated: April 8, 2022)

The electron-like excess observed by the MiniBooNE experiment is explained with a model comprising a new low mass state ($\mathcal{O}(1)$ eV) participating in neutrino oscillations and a new high mass state ($\mathcal{O}(100)$ MeV) that decays to $\nu + \gamma$. Short-baseline oscillation data sets are used to predict the oscillation parameters. Fitting the MiniBooNE energy and scattering angle data, there is a narrow joint allowed region for the decay contribution at 95% CL. The result is a substantial improvement over the single sterile neutrino oscillation model, with $\Delta\chi^2/dof = 19.3/2$ for a decay coupling of 2.8×10^{-7} GeV⁻¹, high mass state of 376 MeV, oscillation mixing angle of 7×10^{-4} and mass splitting of 1.3 eV². This model predicts that no clear oscillation signature will be observed in the FNAL short baseline program due to the low signal-level.

Introduction.—For the past 25 years, anomalies have been observed in short-baseline (SBL) neutrino oscillation experiments. These have been studied under a model called “3+1” that introduces a new non-interacting, hence “sterile,” state with mass of $\mathcal{O}(1)$ eV, in addition to the three known neutrino states in the Standard Model (SM). In this model, $\nu_\mu \rightarrow \nu_e$ appearance, ν_e disappearance, and ν_μ disappearance searches should all point to neutrino oscillations at $L/E \sim 1$ m/MeV, where L is the distance a neutrino of energy E travels, with a consistent set of flavor mixing parameters [1–4]. However, while individually the data appear to fit oscillations, global fits find a small probability that all of the relevant data sets are explained by the same parameters [2, 3], as measured by the Parameter Goodness of Fit (PG) test [5, 6]. In particular, appearance data from the MiniBooNE experiment produces large tension between appearance and disappearance in the 3+1 model. This is because the 3+1 best-fit parameters from the other data sets yield a poor fit to the lowest energy range of the MiniBooNE anomaly [7].

The MiniBooNE anomaly is a 4.8σ excess of electron-like events observed in interactions from a predominantly muon neutrino beam in a Cherenkov detector [8]. Cherenkov detectors cannot distinguish between electromagnetic showers from electrons and photons. Hence, a favored alternative to the 3+1 model has been to introduce MeV-scale heavy neutral leptons (HNLs) that decay via $\mathcal{N} \rightarrow \nu\gamma$ within the detector, where the photon

is then misidentified as an electron [9–17]; see Refs.[18–24] for misidentified di-electron scenarios. These initial studies of \mathcal{N} -decay models describe the MiniBooNE appearance energy distribution well, but omit the 3+1 oscillations predicted from fits to the other anomalies.

In this paper, we explore a combination of the two explanations by fitting the MiniBooNE appearance energy and angle distributions using a combined model, 3+1+ \mathcal{N} -decay. The 3+1 oscillation component is obtained by fitting SBL data sets other than MiniBooNE appearance. We will show that such a model explains the data well, identifying a highly limited range for the four model parameters: the mixing angle, $\sin^2 2\theta$, and mass splitting, Δm^2 , for the oscillation; and the HNL mass, $m_{\mathcal{N}}$, and photon coupling, d , for the decay.

Model.—The combination of an eV-scale and MeV-scale mass states are motivated if the two are members of a family of \mathcal{N}_j where $j = 1, 2, 3$. If the mass splitting are similar to the quark and lepton sector, then the family might also include a keV-scale member [25, 26]. All members may interact with photons at a weak level through a dipole portal mechanism [9, 16]; also known as neutrino magnetic moment [27–32]. Thus, the $\mathcal{N}_1 = \nu_4$ can, in principle, decay, but the lifetime is typically longer than the age of the Universe [28, 33]. The keV mass state, \mathcal{N}_2 , will have a lifetime that is too long to observe through decay in terrestrial experiments but could explain observed X-ray lines [25, 34]. Only the $\mathcal{N} \equiv \mathcal{N}_3$ will decay on length scales observable by SBL experiments. On the other hand, only the eV-scale mass state will have sufficiently small mass splitting with respect to the three known light neutrino states [35–38] to form an observable oscillation pattern. In the 3+1+ \mathcal{N} -decay model, any given SBL experiment may be sensitive to signatures of 3+1 oscillations only, $\mathcal{N} \rightarrow \nu\gamma$ only, or both.

If the maximum energy of the neutrino source is too small to produce the heavier \mathcal{N} state, then the SBL ex-

* sv408@hep.phy.cam.ac.uk

† nwkamp@mit.edu

‡ diaza@mit.edu

§ carguelles@fas.harvard.edu

¶ conrad@mit.edu

** shaevitz@nevis.columbia.edu

†† mauchida@hep.phy.cam.ac.uk

Used to Test	References (Flux Type)	Type of Fit
$\bar{\nu}_e$ disappearance	[39–43] (Reactor)	
ν_e disappearance	[44–46] (Source)	
$\bar{\nu}_\mu \rightarrow \bar{\nu}_e$ appearance	[47, 48] (π/μ DAR)	↑
$\nu_\mu \rightarrow \nu_e$ appearance	[49] (π/μ DIF)	3+1-only
$\bar{\nu}_\mu$ disappearance	[50–53] (π/μ DIF)	↓
ν_μ disappearance	[51, 54–56] (π/μ DIF)	
3 + 1 + \mathcal{N}	[8] (MiniBooNE BNB ν)	\mathcal{N}

TABLE I. Data sets used in this paper. These include reactor, radioactive, decay-at-rest (DAR) and decay-in-flight (DIF) neutrino sources.

periment can observe only 3+1 oscillations. The references for relevant “3+1-only” experiments used in this analysis are provided in Table I (top), and include experiments with anomalies of significance from 2σ to 4.8σ , as well as experiments consistent with null. We use these experiments to determine the oscillation parameters.

As shown in Table I (bottom), we use MiniBooNE data to fit for the \mathcal{N} parameters, given the oscillation parameters from the 3+1-only fit. The MiniBooNE experiment has excesses in three appearance data subsets: neutrino-mode [57], antineutrino mode [58], and with an off-axis beam [59]. All three cases are compatible with either 3+1 or HNL explanations. However, the latter two running modes had low statistics and more limited released information, so we restrict our fit to the neutrino-mode MiniBooNE sample.

Three SBL experiments have relevant limits to \mathcal{N} with mass > 10 MeV. While not appearing directly in the fit, the viable solution must fall outside of these limits. NOMAD and CHARM II were high-energy neutrino experiments with sufficiently short L/E that they were not sensitive to the 3+1 parameters under discussion. The NOMAD analysis searched directly for photons from HNL decay [13]. CHARM II could not differentiate electrons from photons, and the limit is derived from comparing ν_μ -electron elastic scattering (ES) data to the SM prediction [60]. At larger \mathcal{N} masses, which are kinematically inaccessible in the former process, contributions from ν_μ -nucleon up-scattering are also present [21], however have not been computed for CHARM-II due to lack of a detailed analysis. LSND has also released ν_μ -electron scattering results in agreement with the SM, and so this data set allows an HNL limit from LSND [16].

In our model, the production and decay of \mathcal{N}_j is due to a dipole portal interaction between left-handed neutrinos, photons, and right-handed HNLs. The \mathcal{N}_j are added to the SM Lagrangian using the following term [14, 16]:

$$\sum_{j=1}^3 \bar{\mathcal{N}}_j (i\not{\partial} - M_j) \mathcal{N}_j + \sum_{i=1}^3 (d_{i,j} \bar{\nu}_i \sigma_{\mu\nu} F^{\mu\nu} \mathcal{N}_j + h.c.), \quad (1)$$

where the ν_i correspond to the light neutrino mass states, $F^{\mu\nu}$ is the electromagnetic field strength, and the dimension-full d_{ij} couplings control the strength of the

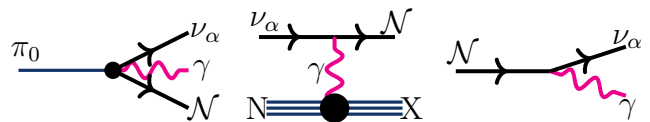


FIG. 1. \mathcal{N} production from π^0 Dalitz decay (left) and ν up-scattering (middle), and decay (right).

electromagnetic interactions between neutrino species, namely the strength of process like $\mathcal{N}_j \rightarrow \nu_i \gamma$.

This leads to two production mechanisms for \mathcal{N}_j : coupling to virtual photons produced in meson decays, such as π^0 , and Primakoff upscattering of active neutrinos to \mathcal{N} as they traverse material. Feynman diagrams for the two production processes are shown in the left and middle of Fig. 1, and decay is shown on the right.

In our analysis, we will consider only production and decay of the third mass state \mathcal{N} . This follows if d is the same for all generations and is found to be sufficiently small, such that up-scattering is rare, because then the small masses of states 1 and 2 lead to lifetimes that are too long to observe decay in an SBL experiment. An alternative explanation if d is found to be large is that the d_{ij} vary with family member, suppressing decays of the first and second mass states. In the decay, the polarization of \mathcal{N} must be considered [61–63]. The photon from a right-handed Dirac \mathcal{N} decay has a $(1 - \cos \theta)$ distribution, where θ is the angle between the \mathcal{N} and photon momentum vectors; conversely, a left-handed Dirac \mathcal{N} will decay with a $(1 + \cos \theta)$ distribution for the photons. Production through an unpolarized virtual, off-shell photon yields an equal combination of right-handed and left-handed \mathcal{N} , leading to an effectively isotropic photon decay distribution. On the other hand, for the case of up-scattering, where the \mathcal{N} is produced from an interaction with a left-handed muon neutrino, the outgoing \mathcal{N} will be right-handed and the $(1 - \cos \theta)$ angular distribution of the photons must be considered. All three new mass states appear in a mixing matrix that relates them to the flavor states. Calling the new flavors s_j , for “sterile” within the SM, the mass and flavor states are related by:

$$\nu_\alpha = \sum_i U_{\alpha i} \nu_j + U_{\alpha 3+i} \mathcal{N}_i, \quad (\alpha = e, \mu, \tau; s_1, s_2, s_3), \quad (2)$$

where $U_{\alpha j}$ is the extended 6×6 neutral-lepton matrix [1].

Oscillation Global Fit.—The 3+1-only data sets are used to restrict the oscillation parameters for the full 3 + 1 + \mathcal{N} -decay fit. We will assume that the largest two mass states are not relevant to oscillations, given their large masses. Therefore, the only relevant squared-mass-splitting Δm^2 is between the lightest mostly sterile and the mostly active states, where the masses of the latter are assumed to be degenerate and negligible. We will concentrate on the 4×4 neutral-lepton-mixing sub-matrix that relates the lightest mass states to their flavor states. For $U_{\alpha k}$, where α is the flavor and k is the

mass state, the mixing angles for the appearance and disappearance oscillation signatures are not independent: $\sin^2 2\theta_{ee} = 4(1 - |U_{e4}|^2)|U_{e4}|^2$ (electron flavor disappearance); $\sin^2 2\theta_{\mu\mu} = 4(1 - |U_{\mu4}|^2)|U_{\mu4}|^2$ (muon flavor disappearance); and $\sin^2 2\theta_{\mu e} = 4|U_{\mu4}|^2|U_{e4}|^2$ (appearance). This implies that the electron and muon flavor disappearance signals must be consistent with the $\nu_\mu \rightarrow \nu_e$ appearance signal, limiting the range of $\sin^2 2\theta_{e\mu}$.

This analysis employs the 3+1 global fitting code described in Ref. [3]. The 3+1-only global fit omits the MiniBooNE neutrino-mode, antineutrino-mode, and off-axis appearance data sets. Otherwise, the experiments described in Section 4.4 of Ref. [3] are included. We have added new disappearance results from the STEREO experiment [43] and updated PROSPECT result [42]. In this update, we have not included the results from NEUTRINO-4 [64], since the collaboration has not provided an appropriate data release. Finally, we have also not included the latest result from IceCube [65, 66], which shows a preferred region at 90% CL compatible with our light sterile neutrino best-fit point, since the collaboration has not provided enough information to reproduce the analysis.

The best-fit parameters are $\Delta m^2 = 1.32 \text{ eV}^2$ and $\sin^2 2\theta_{e\mu} = 6.9 \times 10^{-4}$. In past 3+1 fits, the tension between the appearance and disappearance data sets [3], as measured using the PG test, has been very high, with a probability of 4×10^{-6} (4.5σ) that the data are explained by the same parameters. Without MiniBooNE appearance in the fit, the probability increases to 7×10^{-3} (2.4σ). Thus, the tension is, in large part, due to the MiniBooNE appearance data set, which we hypothesize has the additional component of \mathcal{N} -decay, and, hence, poor agreement with 3+1-only.

MiniBooNE Analysis—In order to fit MiniBooNE data for \mathcal{N} decay, we wrote a Monte Carlo simulation for the production and decay of \mathcal{N} in the Booster Neutrino Beam in neutrino mode. Two processes were included for production: Dalitz-like π^0 decays and Primakoff upscattering $\nu A \rightarrow \mathcal{N} A$. The latter is by far the dominant \mathcal{N} -production mode for $10 \text{ MeV} < m_{\mathcal{N}} < 1000 \text{ MeV}$. Therefore, we have neglected the π^0 decay contribution throughout this study. For the Primakoff mode we generated incident ν_μ and ν_e events from the MiniBooNE neutrino-mode flux [67] and simulated the upscattering rate on both standard upper-continental crust nuclei [68] and the MiniBooNE CH_2 detector medium, using Eq. A6 in Ref. [16] to calculate the total interaction rate and momentum transfer. This process produces a sample of right-hand-polarized \mathcal{N} events which are predominately forward-peaked, due to the $1/t^2$ dependence of the differential cross section.

Simulated \mathcal{N} that enter the MiniBooNE detector were then allowed to decay to produce a photon, taking into account polarization. To incorporate the detector efficiency, eff , we perform a linear fit to the reconstructed

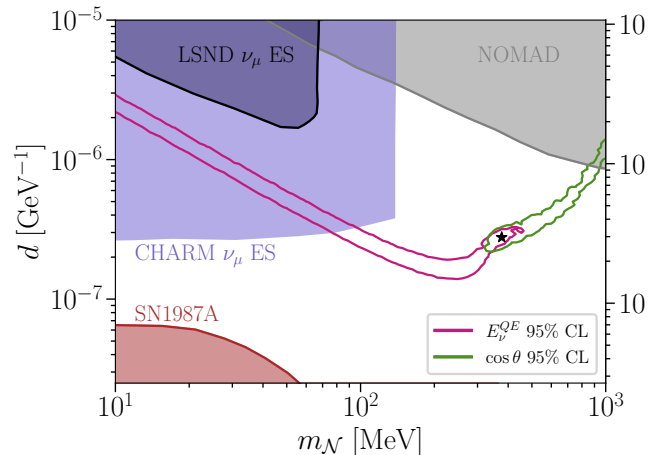


FIG. 2. Preferred regions to explain the MiniBooNE excess in E_ν^{QE} (pink) and $\cos \theta$ (green) as a function of dipole coupling and \mathcal{N} mass. The black star indicates $\{d, m_{\mathcal{N}}\} = \{2.8 \times 10^{-7} \text{ GeV}^{-1}, 376 \text{ MeV}\}$, which lies in the joint 95% CL allowed region for both distributions. Constraints from other experiments are also shown at the 95% CL.

gamma-ray efficiency as a function of true energy [69], $eff = (-0.12 \text{ GeV}^{-1}) * E_{true} + 0.29$, which we use to weight the $\mathcal{N} \rightarrow \nu\gamma$ events. The true energy and angle of the photon are smeared independently according to the resolution given by the MiniBooNE collaboration.

Ideally one would fit the background-subtracted 2-D distribution of visible energy, E_v , vs. scattering angle, θ , of the MiniBooNE events to the prediction from $3 + 1 + \mathcal{N}$ -decay. However, the systematic errors for this distribution has not been released by MiniBooNE. The systematic errors are only available for E_ν^{QE} , which is a combination of E_v and θ , and is given by [70]

$$E_\nu^{QE} = \frac{2(M_n - B)E_v - ((M_n - B)^2 + M_e^2 - M_p^2)}{2((M_n - B) - E_v + \sqrt{(E_v^2 - M_e^2) \cos \theta})}, \quad (3)$$

where M_n , M_p , and M_e are the neutron, proton and electron masses, and B is the binding energy of carbon. This formula accurately describes the neutrino energy in the case of two-body charged current neutrino scattering with no final state interactions, assuming the neutrinos enter the detector along the axis from which θ is measured, thus is applicable to the component of the excess that is due to oscillations. Though E_ν^{QE} has no physical meaning when applied to the photons from \mathcal{N} decay, the decay kinematics cause most events to be show up at low E_ν^{QE} . We have performed a fit to the MiniBooNE excess in E_ν^{QE} using statistical and systematic uncertainties. We have also separately fit the scattering angle distribution, although only statistical uncertainty is available in this case.

To isolate the decay component, we subtract the predicted contribution of the oscillation component determined from the global fits. The remaining excess is

fit to the model for production, decay, and observation in the detector as described above. Fig. 2 shows confidence regions for both fits in $\{d, m_{\mathcal{N}}\}$ parameter space computed assuming Wilks' theorem with two degrees of freedom is valid for the test statistic defined as $\chi^2(d, m) - \min_{d, m}(\chi^2(d, m))$ [71]. We find a region of parameter space consistent with both distributions at the 95% CL near $d = 3 \times 10^{-7} \text{ GeV}^{-1}$ and $m_{\mathcal{N}} = 400 \text{ MeV}$.

Results.—Fig. 2 shows that the allowed regions from MiniBooNE fits are substantially lower in d than the NOMAD or LSND limits. The overlapping solution is also at substantially higher $m_{\mathcal{N}}$ than is kinematically allowed for LSND. Supernova results [16] set limits in a band from approximately $d = 10^{-7}$ to $10^{-11} \text{ GeV}^{-1}$, which is below the solution we find for MiniBooNE. Thus, the result lies in a window of allowed parameters.

We now consider an example HNL decay contribution for $d = 2.8 \times 10^{-7} \text{ GeV}^{-1}$ and $m_{\mathcal{N}} = 376 \text{ MeV}$, indicated by the star in Fig. 2. This point gives the best fit to the E_{ν}^{QE} distribution within the joint 95% CL allowed region from the E_{ν}^{QE} and $\cos\theta$ fits. Table II shows the χ^2 values for the 3+1 and 3+1+ \mathcal{N} -decay fits to both distributions, indicating significant improvement for the 3+1+ \mathcal{N} -decay model. The global oscillation fit gives tight constraints requiring $\Delta m^2 \approx 1.32 \text{ eV}^2$, but allows values of $\sin^2 2\theta_{\mu e} \in [3 \times 10^{-4}, 2 \times 10^{-3}]$ at the 90% CL. The same \mathcal{N} decay fit procedure outlined above has been performed for each end of the allowed $\sin^2 2\theta_{\mu e}$ range. In each case we have again chosen the $\{d, m_{\mathcal{N}}\}$ point that best fits the E_{ν}^{QE} distribution within the joint 95% CL region. The χ^2 values for these fits are also given in Table II, indicating a preference for a smaller oscillation contribution in MiniBooNE in order to explain both the $\cos\theta$ and E_{ν}^{QE} distributions via $\mathcal{N} \rightarrow \nu\gamma$. Table II also gives the χ^2 values for the null case, with neither eV-scale oscillations nor HNL decay.

Parameters	χ^2/dof			
	3 + 1 + \mathcal{N}		3 + 1	
$(\sin^2 2\theta, d, m_{\mathcal{N}})$	E_{ν}^{QE}	$\cos\theta$	E_{ν}^{QE}	$\cos\theta$
(0.30, 3.1, 376)	5.7/8	32.1/18	30.5/10	86.4/20
(0.69, 2.8, 376)	7.9/8	31.4/18	27.3/10	71.8/20
(2.00, 5.6, 35)	20.2/8	36.7/18	27.6/10	40.8/20
(0, 0, 0)	34.1/10	99.4/20	same	same

TABLE II. χ^2/dof values for 3+1 and 3+1+ \mathcal{N} -decay models obtained by comparing expectations to the MiniBooNE excess in E_{ν}^{QE} and $\cos\theta$. The parameters in column one refer to $(\sin^2 2\theta_{\mu e} \times 10^{-3}, d \times 10^{-7} [\text{GeV}^{-1}], m_{\mathcal{N}} [\text{MeV}])$. The mass splitting is 1.32 eV^2 in all cases. The null case (no oscillations and no HNL decay) is also shown in the last row.

Fig. 3 presents the MiniBooNE excess in E_{ν}^{QE} (left) and $\cos\theta$ (right) compared with the model prediction. This figure includes both the global fit oscillation contribution for $\Delta m^2 = 1.3 \text{ eV}^2$ and $\sin^2 2\theta_{ee} = 6.9 \times 10^{-7}$, and HNL decay contribution for $d = 2.8 \times 10^{-7} \text{ GeV}^{-1}$

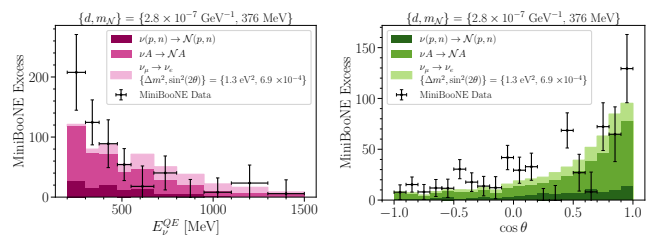


FIG. 3. E_{ν}^{QE} (left) and $\cos\theta$ (right) distributions of the MiniBooNE excess for a representative point of the 3 + 1 + \mathcal{N} -decay model. The error bars on the energy distribution include systematic and statistical errors, while for the angular distribution only statistical errors are included.

and $m_{\mathcal{N}} = 376 \text{ MeV}$. Good agreement is observed for both distributions.

Along with energy and angle, it is essential that the model be consistent with the recently published timing distribution of the MiniBooNE events with respect to the proton-beam bunch. It has been shown that the excess events occur within $\pm 4 \text{ ns}$ of the observed ν_{μ} events. The time of flight depends on the location at which the HNL is produced. For the preferred mass range of $m_{\mathcal{N}} \sim 400 \text{ MeV}$, the majority of upscattering events happen within the MiniBooNE detector. This leads to decay lengths of $\mathcal{O}(10 \text{ cm})$ and subsequent timing delays of $< 2 \text{ ns}$, well within the MiniBooNE constraint.

Conclusion.—This analysis has explored a 3+1+ \mathcal{N} -decay model through fits to the 3+1-only and MiniBooNE-neutrino-mode data sets. The former yields best-fit oscillation parameters of $\Delta m^2 = 1.3 \text{ eV}^2$ and $\sin^2 2\theta_{e\mu} = 6.9 \times 10^{-4}$. The latter narrows the best-fit decay parameters from HNL dipole portal decay to 300 to 400 MeV mass and 2.5×10^{-7} to $3.5 \times 10^{-7} \text{ GeV}^{-1}$ coupling ranges. This model produces a $\Delta\chi^2/\text{dof}$ improvement of 19.3/2 (40.3/2) above the global 3+1 scenario for the fit to the MiniBooNE energy (angular) distributions. This very large improvement in $\Delta\chi^2$ motivates a more detailed analysis by MiniBooNE. Ideally, the experiment will perform a joint fit to the two-dimensional visible energy and angle distribution, using a full covariance matrix. This will allow a more detailed description of \mathcal{N} production and reconstruction of decays using the internal collaboration tools.

Our model also makes very specific predictions for the experiments now running in Fermilab's short-baseline Neutrino Program [72]. These experiments make use of liquid argon time projection chambers (LArTPCs) that can separate photon showers from electron showers with $\sim 85\%$ accuracy [73, 74]. Because the experiments run in the same beamline and are located within $\sim 50 \text{ m}$ of MiniBooNE, the flux is nearly identical. Thus the ratio of oscillation to HNL decay contributions for the far detectors — MicroBooNE and ICARUS — will be very similar to that of the MiniBooNE case presented here,

with $\sim 75\%$ of the excess events predicted to be single photons. The photon signature will have large backgrounds even in an LArTPC detector, especially from neutral current Δ baryon production with decays to one or two photons plus a neutron, as well as photons from neutrino interactions produced outside the detector [75]. However, this background rate will be well constrained from reconstructed Δ -decay events with a proton. Also, the energy-angle correlation of the photon in the decay, which depends strongly on $m_{\mathcal{N}}$, can be used for background rejection since this parameter is predicted to have a narrow range of values. The oscillation rates for MicroBooNE and ICARUS are predicted to be low. Within statistics, we predict that no clear oscillation signature will be observed.

In summary, we have presented a new physics model including neutrino-partners with masses of $\mathcal{O}(1 \text{ eV})$ that participate in oscillations and $\mathcal{O}(100 \text{ MeV})$ that decay to single photons. This model can simultaneously explain the MiniBooNE anomaly and relieve tension in the global experimental picture for 3+1 oscillations. The results indicate very narrow ranges of HNL decay and oscillation parameters; thus this is a highly predictive result that can be further tested by existing experiments in the near future.

ACKNOWLEDGEMENTS

MHS is supported by NSF grant PHY-1707971. NSF grant PHY-1801996 supported CAA, JMC, AD and NWK for this work. Additionally, CAA is supported by the Faculty of Arts and Sciences of Harvard University and NWK is supported by the NSF Graduate Research Fellowship under Grant No. 1745302. We thank the MiniBooNE Collaboration for useful input, and Gabriel Collin and William Louis for comments on the draft of this paper. Finally, we thank Matheus Hostert and Ryan Plestid for useful discussions.

[1] G. Collin, C. Argüelles, J. Conrad, and M. Shaevitz, Phys. Rev. Lett. **117**, 221801 (2016), 1607.00011.
[2] M. Dentler, A. Hernández-Cabezudo, J. Kopp, P. A. Machado, M. Maltoni, I. Martinez-Soler, and T. Schwetz, JHEP **08**, 010 (2018), 1803.10661.
[3] A. Diaz, C. Argüelles, G. Collin, J. Conrad, and M. Shaevitz, Phys. Rept. **884**, 1 (2020), 1906.00045.
[4] S. Böser, C. Buck, C. Giunti, J. Lesgourgues, L. Ludhova, S. Mertens, A. Schukraft, and M. Wurm, Prog. Part. Nucl. Phys. **111**, 103736 (2020), 1906.01739.
[5] M. Maltoni, T. Schwetz, and J. W. F. Valle, Phys. Rev. D **65**, 093004 (2002), hep-ph/0112103.
[6] M. Maltoni and T. Schwetz, Phys. Rev. D **68**, 033020 (2003), hep-ph/0304176.

[7] C. Giunti, M. Laveder, Y. F. Li, and H. W. Long, Phys. Rev. D **88**, 073008 (2013), 1308.5288.
[8] A. Aguilar-Arevalo et al. (MiniBooNE) (2020), 2006.16883.
[9] S. Palomares-Ruiz, S. Pascoli, and T. Schwetz, JHEP **09**, 048 (2005), hep-ph/0505216.
[10] S. Gninenko, Phys. Rev. Lett. **103**, 241802 (2009), 0902.3802.
[11] D. McKeen and M. Pospelov, Phys. Rev. D **82**, 113018 (2010), 1011.3046.
[12] C. Dib, J. C. Helo, S. Kovalenko, and I. Schmidt, Phys. Rev. D **84**, 071301 (2011), 1105.4664.
[13] S. Gninenko, Phys. Lett. B **710**, 86 (2012), 1201.5194.
[14] M. Masip, P. Masjuan, and D. Meloni, JHEP **01**, 106 (2013), 1210.1519.
[15] P. Ballett, S. Pascoli, and M. Ross-Lonergan, JHEP **04**, 102 (2017), 1610.08512.
[16] G. Magill, R. Plestid, M. Pospelov, and Y.-D. Tsai, Phys. Rev. D **98**, 115015 (2018), 1803.03262.
[17] O. Fischer, A. Hernández-Cabezudo, and T. Schwetz, Phys. Rev. D **101**, 075045 (2020), 1909.09561.
[18] E. Bertuzzo, S. Jana, P. A. N. Machado, and R. Zukanovich Funchal (2018), 1808.02500.
[19] E. Bertuzzo, S. Jana, P. A. Machado, and R. Zukanovich Funchal, Phys. Rev. Lett. **121**, 241801 (2018), 1807.09877.
[20] P. Ballett, S. Pascoli, and M. Ross-Lonergan, Phys. Rev. D **99**, 071701 (2019), 1808.02915.
[21] C. A. Argüelles, M. Hostert, and Y.-D. Tsai, Phys. Rev. Lett. **123**, 261801 (2019), 1812.08768.
[22] P. Ballett, M. Hostert, and S. Pascoli, Phys. Rev. **D99**, 091701 (2019), 1903.07590.
[23] P. Ballett, M. Hostert, and S. Pascoli, Phys. Rev. D **101**, 115025 (2020), 1903.07589.
[24] A. Abdullahi, M. Hostert, and S. Pascoli (2020), 2007.11813.
[25] M. Drewes et al., JCAP **01**, 025 (2017), 1602.04816.
[26] A. Abada, K. N. Abazajian, A. Abdullahi, S. K. Agarkar, J. A. Aguilar, W. Altmannshofer, C. A. Argüelles, A. B. Balantekin, G. Barenboim, B. Batell, et al., *Opportunities and signatures of non-minimal heavy neutral leptons*, Letter of Interest submitted to the Snowmass2021 (2020), https://www.snowmass21.org/docs/files/summaries/NF/SNOWMASS21-NF2_NF3-EF9_EF0-RF4_RF6-CF1_CFO-TF8_TF11_Matheus_Hostert-041.pdf.
[27] K. Fujikawa and R. Shrock, Phys. Rev. Lett. **45**, 963 (1980).
[28] P. B. Pal and L. Wolfenstein, Phys. Rev. D **25**, 766 (1982).
[29] R. E. Shrock, Nucl. Phys. B **206**, 359 (1982).
[30] M. Dvornikov and A. Studenikin, Phys. Rev. D **69**, 073001 (2004), hep-ph/0305206.
[31] C. Giunti and A. Studenikin, Rev. Mod. Phys. **87**, 531 (2015), 1403.6344.
[32] V. Brdar, A. Greljo, J. Kopp, and T. Opferkuch, JCAP **01**, 039 (2021), see arXiv version v3 for updated constraint plot summary., 2007.15563.
[33] J. F. Nieves, Phys. Rev. D **28**, 1664 (1983).
[34] K. N. Abazajian, Phys. Rept. **711-712**, 1 (2017), 1705.01837.
[35] M. Tanabashi et al. (Particle Data Group), Phys. Rev. D **98**, 030001 (2018).
[36] I. Esteban, M. Gonzalez-Garcia, A. Hernandez-Cabezudo, M. Maltoni, and T. Schwetz, JHEP **01**, 106

- (2019), 1811.05487.
- [37] P. de Salas, D. Forero, C. Ternes, M. Tortola, and J. Valle, *Phys. Lett. B* **782**, 633 (2018), 1708.01186.
- [38] F. Capozzi, E. Lisi, A. Marrone, D. Montanino, and A. Palazzo, *Nucl. Phys. B* **908**, 218 (2016), 1601.07777.
- [39] Y. Declais et al., *Nucl. Phys.* **B434**, 503 (1995).
- [40] Y. J. Ko et al. (NEOS), *Phys. Rev. Lett.* **118**, 121802 (2017), 1610.05134.
- [41] I. Alekseev et al. (DANSS), *Phys. Lett.* **B787**, 56 (2018), 1804.04046.
- [42] M. Andriamirado, A. B. Balantekin, H. R. Band, C. D. Bass, D. E. Bergeron, D. Berish, N. S. Bowden, J. P. Brodsky, C. D. Bryan, T. Classen, et al. (PROSPECT Collaboration), *Phys. Rev. D* **103**, 032001 (2021), URL <https://link.aps.org/doi/10.1103/PhysRevD.103.032001>.
- [43] H. Almazán, L. Bernard, A. Blanchet, A. Bonhomme, C. Buck, P. del Amo Sanchez, I. El Atmani, J. Haser, F. Kandzia, S. Kox, et al. (STEREO Collaboration), *Phys. Rev. D* **102**, 052002 (2020), URL <https://link.aps.org/doi/10.1103/PhysRevD.102.052002>.
- [44] J. M. Conrad and M. H. Shaevitz, *Phys. Rev.* **D85**, 013017 (2012), 1106.5552.
- [45] F. Kaether, W. Hampel, G. Heusser, J. Kiko, and T. Kirsten, *Phys. Lett.* **B685**, 47 (2010), 1001.2731.
- [46] J. N. Abdurashitov et al. (SAGE), *Phys. Rev.* **C80**, 015807 (2009), 0901.2200.
- [47] A. Aguilar-Arevalo et al. (LSND), *Phys. Rev. D* **64**, 112007 (2001), hep-ex/0104049.
- [48] B. Armbruster et al. (KARMEN), *Phys. Rev.* **D65**, 112001 (2002), hep-ex/0203021.
- [49] P. Astier et al. (NOMAD), *Phys. Lett.* **B570**, 19 (2003), hep-ex/0306037.
- [50] G. Cheng et al. (MiniBooNE, SciBooNE), *Phys. Rev.* **D86**, 052009 (2012), 1208.0322.
- [51] I. E. Stockdale et al., *Phys. Rev. Lett.* **52**, 1384 (1984).
- [52] P. Adamson et al. (MINOS), *Phys. Rev. Lett.* **108**, 191801 (2012), 1202.2772.
- [53] P. Adamson et al. (MINOS), *Phys. Rev.* **D84**, 071103 (2011), 1108.1509.
- [54] K. B. M. Mahn et al. (SciBooNE, MiniBooNE), *Phys. Rev.* **D85**, 032007 (2012), 1106.5685.
- [55] F. Dydak et al., *Phys. Lett.* **134B**, 281 (1984).
- [56] P. Adamson et al. (MINOS), *Phys. Rev. Lett.* **117**, 151803 (2016), 1607.01176.
- [57] A. A. Aguilar-Arevalo et al. (MiniBooNE), *Phys. Rev. Lett.* **98**, 231801 (2007), 0704.1500.
- [58] A. A. Aguilar-Arevalo et al. (MiniBooNE), *Phys. Rev. Lett.* **110**, 161801 (2013), 1303.2588.
- [59] P. Adamson et al. (MiniBooNE, MINOS), *Phys. Rev. Lett.* **102**, 211801 (2009), 0809.2447.
- [60] P. Coloma, P. A. N. Machado, I. Martinez-Soler, and I. M. Shoemaker, *Phys. Rev. Lett.* **119**, 201804 (2017), 1707.08573.
- [61] J. A. Formaggio, J. M. Conrad, M. Shaevitz, A. Vaitaitis, and R. Drucker, *Phys. Rev. D* **57**, 7037 (1998).
- [62] A. Baha Balantekin and B. Kayser, *Ann. Rev. Nucl. Part. Sci.* **68**, 313 (2018), 1805.00922.
- [63] A. de Gouvea, P. J. Fox, B. J. Kayser, and K. J. Kelly (2021), 2104.05719.
- [64] A. P. Serebrov et al. (NEUTRINO-4), *Pisma Zh. Eksp. Teor. Fiz.* **109**, 209 (2019), 1809.10561.
- [65] M. Aartsen et al. (IceCube), *Phys. Rev. Lett.* **125**, 141801 (2020), 2005.12942.
- [66] M. Aartsen et al. (IceCube), *Phys. Rev. D* **102**, 052009 (2020), 2005.12943.
- [67] A. A. Aguilar-Arevalo, C. E. Anderson, A. O. Bazarko, S. J. Brice, B. C. Brown, L. Bugel, J. Cao, L. Coney, J. M. Conrad, D. C. Cox, et al., *Physical Review D* **79** (2009), ISSN 1550-2368, URL <http://dx.doi.org/10.1103/PhysRevD.79.072002>.
- [68] F. W. Clarke and H. S. Washington, *Tech. Rep.* (1924), URL <http://pubs.er.usgs.gov/publication/pp127>.
- [69] Z. Pavlovic, R. Van de Water, and S. Zeller, *Tech. Rep.* (2012).
- [70] A. A. Aguilar-Arevalo, B. C. Brown, J. M. Conrad, R. Dharmapalan, A. Diaz, Z. Djurcic, D. A. Finley, R. Ford, G. T. Garvey, S. Gollapinni, et al. (MiniBooNE Collaboration), *Phys. Rev. D* **103**, 052002 (2021), URL <https://link.aps.org/doi/10.1103/PhysRevD.103.052002>.
- [71] S. S. Wilks, *The Annals of Mathematical Statistics* **9**, 60 (1938), URL <https://doi.org/10.1214/aoms/1177732360>.
- [72] M. Antonello et al. (MicroBooNE, LAr1-ND, ICARUS-WA104) (2015), 1503.01520.
- [73] C. Adams, M. Alrashed, R. An, J. Anthony, J. Asaadi, A. Ashkenazi, S. Balasubramanian, B. Baller, C. Barnes, G. Barr, et al., *Journal of Instrumentation* **15**, P02007–P02007 (2020), ISSN 1748-0221, URL <http://dx.doi.org/10.1088/1748-0221/15/02/P02007>.
- [74] R. Acciarri, C. Adams, J. Asaadi, B. Baller, T. Bolton, C. Bromberg, F. Cavanna, E. Church, D. Edmunds, A. Ereditato, et al. (ArgoNeuT Collaboration), *Phys. Rev. D* **95**, 072005 (2017), URL <https://link.aps.org/doi/10.1103/PhysRevD.95.072005>.
- [75] M. Collaboration (2020), URL <https://microboone.fnal.gov/wp-content/uploads/MICROBOONE-NOTE-1087-PUB.pdf>.
- [76] A. A. Aguilar-Arevalo, C. E. Anderson, A. O. Bazarko, S. J. Brice, B. C. Brown, L. Bugel, J. Cao, L. Coney, J. M. Conrad, D. C. Cox, et al. (MiniBooNE Collaboration), *Phys. Rev. D* **79**, 072002 (2009), URL <https://link.aps.org/doi/10.1103/PhysRevD.79.072002>.
- [77] P. deNiverville, C.-Y. Chen, M. Pospelov, and A. Ritz, *Phys. Rev. D* **95** (2017), 1609.01770.

Supplemental Material

FURTHER EXPLANATION OF THE MINIBOONE \mathcal{N} SIMULATION

Primakoff Upscattering Simulation

In order to simulate the Primakoff process $\nu A \rightarrow \mathcal{N}A$ for a given dipole d coupling and HNL mass $m_{\mathcal{N}}$, we first generated a sample of 5×10^5 ν_{μ} and ν_e events with energies according to the MiniBooNE neutrino-mode flux from [67] and initial azimuthal angles generated randomly in $\cos\theta$ within a cone encompassing the MiniBooNE detector. We chose a scattering location uniformly in column density. For the purposes of this study, we have taken the detector to be a sphere of CH_2 with a radius of 6.1 m, surrounded by a concentric sphere of air with radius 9.1 m, intended to represent the detector hall. The rest of the volume is taken to be standard upper-continental crust. We next select a nucleus for the scattering event according to atomic abundances and scattering cross sections. If the scattering event took place in the dirt, we use atomic abundances from [68], which are reproduced in Table 1. Upscattering events inside the MiniBooNE detector happen exclusively off of CH_2 . Events almost never happen in the air surrounding MiniBooNE due to the low density. Scattering cross sections are calculated by numerically integrating the differential cross section, adapted from Ref. [32]:

$$\begin{aligned} \frac{d\sigma}{dt} = \frac{2\alpha d^2}{m} & \left[F_1^2(t) \left(\frac{1}{E_r} - \frac{1}{E_{\nu}} + m_{\mathcal{N}}^2 \frac{E_r - 2E_{\nu} - M}{4E_{\nu}^2 E_r M} + m_{\mathcal{N}}^4 \frac{E_r - M}{8E_{\nu}^2 E_r^2 M^2} \right) \right. \\ & \left. + \frac{F_2^2(t)}{2M} \left(\frac{2M}{E_{\nu}} ((2E_{\nu} - E_r)^2 - 2E_r M) + m_{\mathcal{N}}^2 \frac{E_r - 4E_{\nu}}{E_{\nu}^2} + \frac{m_{\mathcal{N}}^4}{E_{\nu}^2 E_r} \right) \right], \end{aligned} \quad (\text{A1})$$

where α is the fine structure constant, d is the dipole coupling, E_{ν} is the SM neutrino energy, $m_{\mathcal{N}}$ is the mass of the heavy neutrino, M is the target mass, $t = -(p_{\mathcal{N}} - p_{\nu})^2$ is the momentum transfer, $E_r = -t/2M$ is the target recoil energy, and $F_{1/2}(t)$ are the charge/magnetic target form factors, respectively. Note that the term proportional to $E_r m_{\mathcal{N}}^4$ in the F_1 line only exists for spinless nuclei, and must be replaced for nonzero spin nuclei [14]. In the case of coherent scattering off of a nucleus, F_1 receives a Z^2 enhancement and is therefore dominant over F_2 ; which has therefore been neglected for this study. Here F_1 is given by the dipole approximation

$$F_1^A = \frac{1}{(1 + (r_A^2 q^2)/12)^2}, \quad (\text{A2})$$

where r_A is the nuclear radius of the target. In the case of inelastic scattering off of nucleons, the form factors are calculated by solving the following system of equations, repeated here from Appendix A of Ref. [16].

$$\begin{aligned} G_E^{\{p,n\}} &= F_1^{\{p,n\}} - \frac{Q^2}{4m_{\{p,n\}}^2} F_2^{\{p,n\}} = \{G_D, 0\}, \\ G_E^{\{p,n\}} &= F_1^{\{p,n\}} - \frac{Q^2}{4M^2} F_2^{\{p,n\}} = \mu_{\{p,n\}} G_D, \\ G_D &= \frac{1}{(1 + Q^2/0.71 \text{ GeV}^2)^2}, \\ \mu_{\{p,n\}} &= \{2.793, -1.913\}. \end{aligned} \quad (\text{A3})$$

The total cross section for scattering off of a nuclear target A is given by the incoherent sum of the nuclear and nucleon scattering cross sections, namely

$$\sigma_A = Z^2 \int_{t_{min}}^{t_{max}} \frac{d\sigma_{\nu A \rightarrow \mathcal{N}A}}{dt} dt + Z \int_{t_{min}}^{t_{max}} \frac{d\sigma_{\nu p \rightarrow \mathcal{N}p}}{dt} dt + (A - Z) \int_{t_{min}}^{t_{max}} \frac{d\sigma_{\nu n \rightarrow \mathcal{N}n}}{dt} dt, \quad (\text{A4})$$

where the lower bounds for each integral are given in Appendix C of Ref. [16] and the upper bounds are calculated by requiring physical scattering angles $|\cos(\theta)| < 1$. From this we calculate the probability of scattering off a given nucleus A_k (with atomic fractional abundance in dirt/air/ CH_2 F_k) as

$$P_k = \frac{F_k \sigma_{A_k}}{\sum_{k'} F_{k'} \sigma_{A_{k'}}}. \quad (\text{A5})$$

At this stage, we decide whether each up-scattering event occurred coherently off of the nucleus or inelastically off of a proton or neutron by considering the relative cross sections. We then pull a random momentum transfer from Eq. A1. Once we have chosen a value for t , the heavy neutrino energy and scattering angle are fixed [14]:

$$E_{\mathcal{N}} = E_{\nu} - E_r \quad (\text{A6})$$

$$\cos(\theta) = \frac{E_{\nu} - E_r - ME_r/E_{\nu} - m_{\mathcal{N}}^2/2E_{\nu}}{\sqrt{E_{\nu}^2 + E_r^2 - 2E_{\nu}E_r - m_{\mathcal{N}}^2}}. \quad (\text{A7})$$

The $1/t^2$ dependence of Eq. A1 creates a preference for $E_{\mathcal{N}} \approx E_{\nu}$ and $\cos(\theta) \approx 1$. At this stage, if the scattering angle of the \mathcal{N} is greater than the solid angle of the MiniBooNE detector (considering the scattering location), the event is rejected. If not, we multiply the existing weights by the probability that the heavy neutrino decays via $\mathcal{N} \rightarrow \nu\gamma$ in MiniBooNE, which is given by the following expression [16]:

$$P_{decay} = \exp\left(\frac{-L_{enter}}{L_{decay}}\right) - \exp\left(\frac{-L_{exit}}{L_{decay}}\right) \quad (\text{A8})$$

$$L_{decay} = 4\pi\hbar c \frac{\beta E_{\mathcal{N}}}{d^2(m_{\mathcal{N}}c)^4}, \quad (\text{A9})$$

where $L_{enter/exit}$ denote the distance between the creation point of the HNL and the entry/exit point in the MiniBooNE detector, respectively. The culmination of this simulation chain is a weighted sample of \mathcal{N} events which come from the Primakoff upscattering process and decay in the MiniBooNE detector. The last remaining step is to calculate the POT required to get $N = 5 \times 10^5$ up-scattering events along the BNB beamline. This will depend on the dipole coupling and heavy neutrino mass in general, and can be calculated using

$$N = \text{POT} \int_{E_{\nu}=0}^{10 \text{ GeV}} dE_{\nu} \phi(E_{\nu}) \sum_{\text{targets } A} \sigma_A(E_{\nu}) n_A, \quad (\text{A10})$$

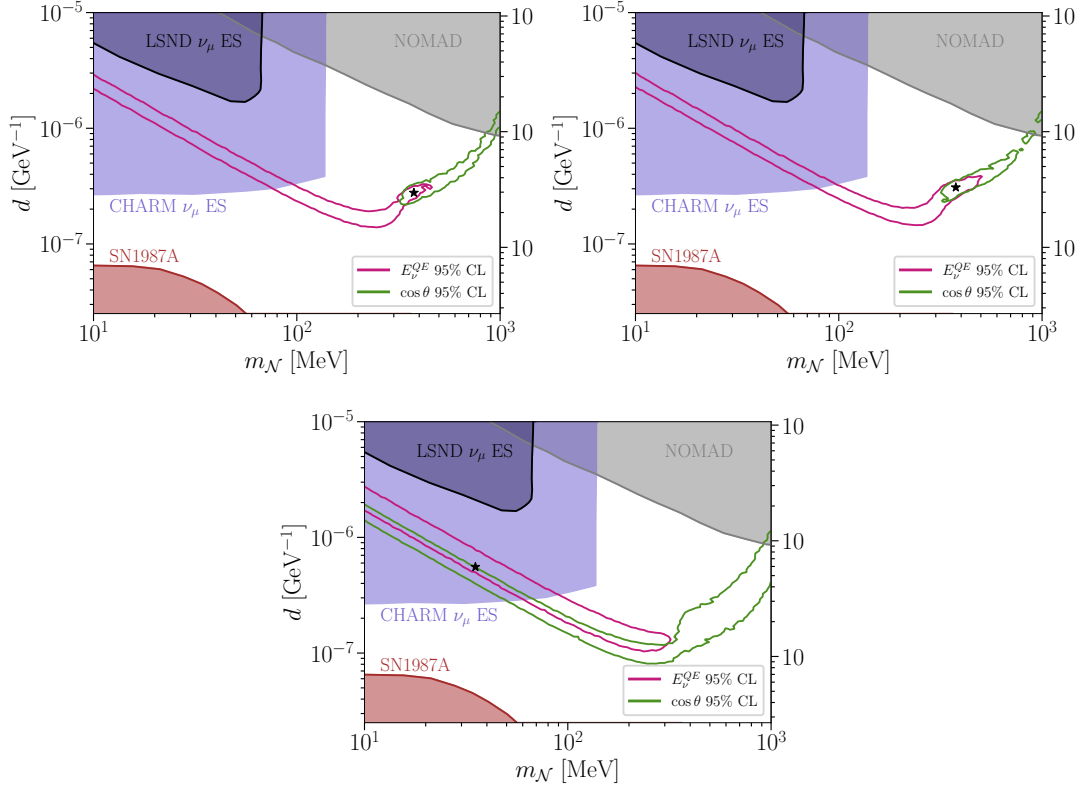
where $\phi(E_{\nu})$ [ν/POT] is again the neutrino flux in MiniBooNE [67], σ_A [cm^2] is the total upscattering cross section for nuclear target A , and n_A [$\text{nuclei}/\text{cm}^2$] is the column density for A along the beamline.

Figure 1 shows the energy/angular fit 95% CL allowed regions in $\{d, m_{\mathcal{N}}\}$ parameter space for the three $\sin^2 2\theta$ values considered in Table II. One can see that the overlap region between the two fits becomes less strict for larger oscillation contributions. This is partially because larger oscillation contributions give a poorer fit to the MiniBooNE excess, as shown by the $\Delta\chi^2$ plots in Figure 2. Here one can see that for the largest $\sin^2 2\theta$, there is no longer a closed contour in either the E_{ν}^{QE} or $\cos\theta$ fit at 3σ CL. Figure 3 shows each of the E_{ν}^{QE} and $\cos\theta$ predictions from Table II compared with the MiniBooNE excess. These plots further indicate a preference for a smaller eV -scale oscillation contribution (considering global best-fit oscillation parameters) in order to fit MiniBooNE.

Finally, we consider the timing delay distribution for HNL decays in the MiniBooNE detector. The timing delay is defined as the time between HNL production and decay minus the same time it would take for a speed of light neutrino to travel the same distance. Figure 4 shows this delay for the three different oscillation amplitude cases, indicating timing delays small enough to be consistent with the MiniBooNE excess timing distribution [8].

Nucleus	Z	A	Crust Mass Fraction	Crust Atomic Fraction	Nuclear Radius [MeV^{-1}]
O	8	16	0.466	0.627	0.00218
Si	14	28	0.277	0.213	0.00252
Al	13	27	0.081	0.065	0.00247
Fe	26	56	0.05	0.019	0.00301
Ca	20	40	0.037	0.02	0.00281
K	19	39	0.027	0.015	0.00277
Na	11	23	0.026	0.024	0.00241
Mg	12	24	0.015	0.013	0.00247
Ti	22	48	0.004	0.002	0.0029
P	15	31	0.001	0.001	0.00257

SUPPL. TABLE I. Relevant parameters of the ten most abundant nuclei in the Earth's upper crust according to [68]



SUPPL. FIG. 1. 95% CL allowed regions in HNL dipole model parameter space from energy and angular fits to the MiniBooNE excess, considering an oscillation contribution with $\Delta m^2 = 1.3 \text{ eV}^2$ and three different amplitudes: $\sin^2 2\theta = 6.9 \times 10^{-4}$ (top left), $\sin^2 2\theta = 3 \times 10^{-4}$ (top right), and $\sin^2 2\theta = 2 \times 10^{-3}$ (bottom).

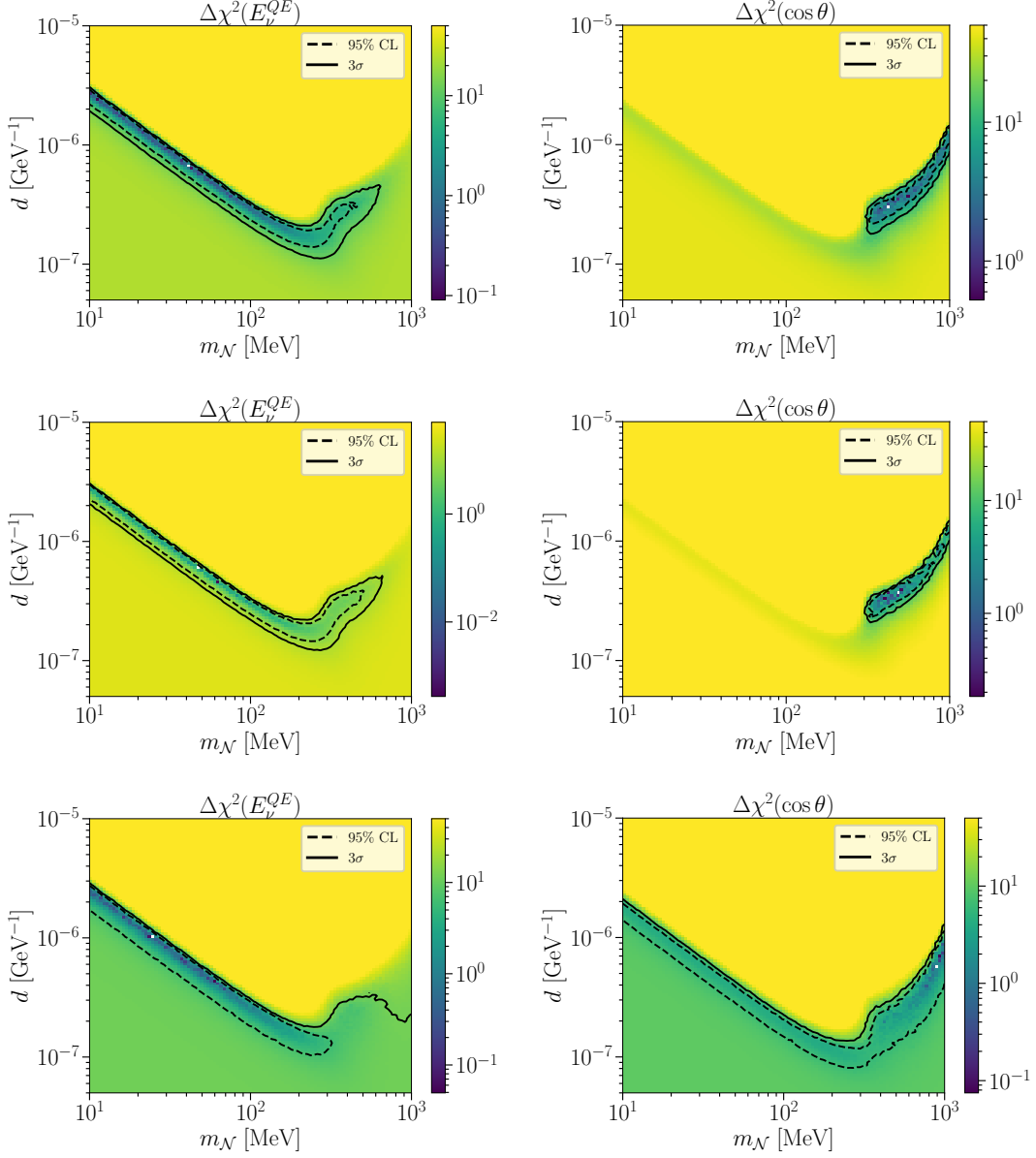
Meson Decay Simulation

The π^0 s have been simulated using a Sanford-Wang (SW) parametrization with π^0 distribution calculated as the average between the π^+ and π^- distributions with coefficients taken from [76]. A rejection sampling from previous studies [77] has been used to simulate momenta $p_{\pi^0} \in [0, 8] \text{ GeV}$, emission angles with respect to the direction of the beam $\theta_{\pi^0} \in [0, \frac{\pi}{2}]$, and angle $\phi_{\pi^0} \in [0, 2\pi]$ of π^0 produced at the source in lab frame. Four-momentum vectors have been created with the aforementioned triplets p_{π^0} , θ_{π^0} , and ϕ_{π^0} according to $p_{\pi^0}^\mu = (E_{\pi^0}, p_{\pi^0} [\cos(\phi_{\pi^0}) \sin(\theta_{\pi^0}), \sin(\phi_{\pi^0}) \sin(\theta_{\pi^0}), \cos(\theta_{\pi^0})])$. A decay probability P_{decay} has been associated to each π^0 according to Eq. A8. In this study, \mathcal{N} have been created via the three body Dalitz-like decay $\pi^0 \rightarrow \mathcal{N} + \nu + \gamma$. Assuming ν to be massless, the energy $E_{\mathcal{N}}$ in the π^0 rest frame has been constrained to be $E_{\mathcal{N}} \in (m_{\mathcal{N}}, \frac{m_{\pi^0}^2 + m_{\mathcal{N}}^2}{2m_{\pi^0}})$ and the differential branching ratio in the π^0 rest frame for each \mathcal{N} has been evaluated using Eq. A.10 in [16]. The simulated \mathcal{N} have been subsequently boosted to the lab frame of the π^0 . Considering the channel $\mathcal{N} \rightarrow \gamma + \nu$ with a massless ν , the γ has been simulated assuming their energies $E_\gamma = \frac{m_{\mathcal{N}}}{2}$, emission angle $\cos(\theta_\gamma) \in [-1, 1]$, angle $\phi_\gamma \in [0, 2\pi]$, and associated four-momentum vectors to be $p_\gamma^\mu = (E_\gamma, p_\gamma [\cos(\phi_\gamma) \sin(\theta_\gamma), \sin(\phi_\gamma) \sin(\theta_\gamma), \cos(\theta_\gamma)])$. The resulting γ s have then been boosted to the lab frame of the \mathcal{N} and multiplied by a normalization constant $N_{const} = \frac{N_{\pi^0}}{N_{sim}}$. $N_{\pi^0} = 1.17 \times 10^{21}$ is the number of π^0 produced in neutrino mode over the lifetime of MiniBooNE for 18.75×10^{20} POT [8] and a π^0 multiplicity per POT 0.9098 [16]. N_{sim} is the effective number of π^0 decays actually simulated.

FURTHER DISCUSSION ON THE FITS

This Appendix provides further information on the fit results presented in this paper.

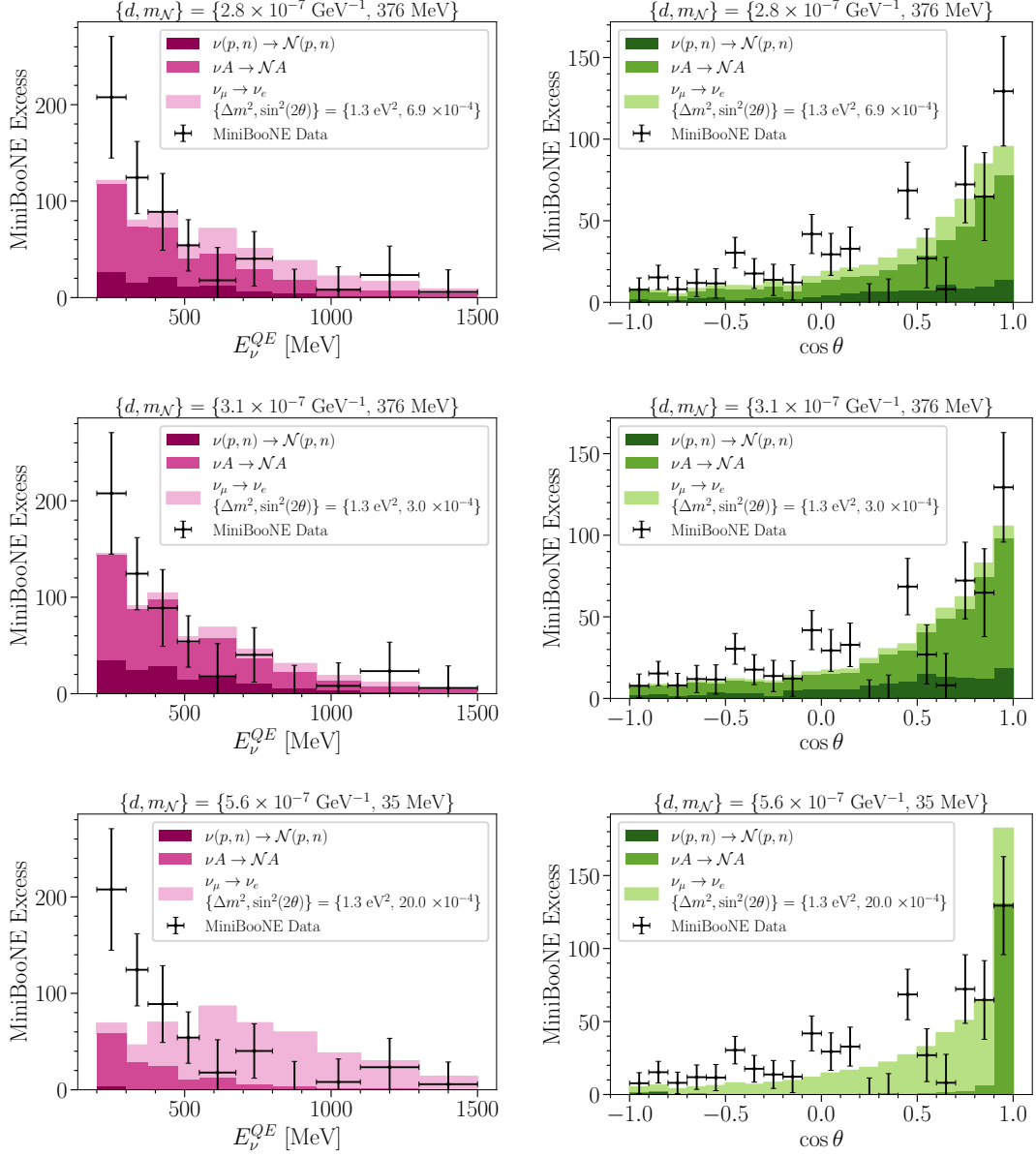
Table II provides a table of the experimental results used in the fits, with references. Notation in Column 3 refers



SUPPL. FIG. 2. Maps of $\Delta\chi^2 = \chi^2(d, m_{\mathcal{N}}) - \min_{\{d, \mathcal{N}\}} \chi^2(d, m_{\mathcal{N}})$ in HNL dipole model parameter space for the energy (left) and angular (right) fits to the MiniBooNE excess, considering an oscillation contribution with $\Delta m^2 = 1.3 \text{ eV}^2$ and three different amplitudes: $\sin^2 2\theta = 6.9 \times 10^{-4}$ (top), $\sin^2 2\theta = 3 \times 10^{-4}$ (middle), and $\sin^2 2\theta = 2 \times 10^{-3}$ (bottom).

to electron flavor disappearance, muon flavor disappearance, and muon-to-electron flavor appearance for neutrinos and antineutrinos. The last two columns indicate the data sets used in the fits to the new $3 + 1 + \mathcal{N}$ model. This model has two contributions: the oscillation contribution, established through a $3+1$ oscillation fit to experiments in Column 3 and the \mathcal{N} decay fit which is established through a fit to the MiniBooNE 2020 data set only, as indicated in Column 4. This omits MiniBooNE (BNB) antineutrino data and MiniBooNE (NuMI) data from the \mathcal{N} decay fit, which have anomalous signals consistent with MiniBooNE (BNB) neutrino data, but at low statistics and with high backgrounds. Including these requires additional development of Monte Carlo beamline simulations, and the modest results will not change the conclusion of this paper, thus we conclude this is beyond the scope of this article.

Below, we provide the results of the oscillations-only global fits using the data indicated in Table II. A thorough description of the fitting process is provided in Ref. [3]. In addition to the experiments listed in Ref. [3], we have updated the MiniBooNE (BNB) neutrino appearance data set [70], updated the PROSPECT antineutrino disappearance data



SUPPL. FIG. 3. Example HNL dipole model predictions for the energy (left) and angular (right) distributions compared with the MiniBooNE excess, considering an oscillation contribution with $\Delta m^2 = 1.3 \text{ eV}^2$ and three different amplitudes: $\sin^2 2\theta = 6.9 \times 10^{-4}$ (top), $\sin^2 2\theta = 3 \times 10^{-4}$ (middle), and $\sin^2 2\theta = 2 \times 10^{-3}$ (bottom). The specific d and m_N values shown here come from Table II.

set [42], and introduced the STEREO antineutrino disappearance data set.

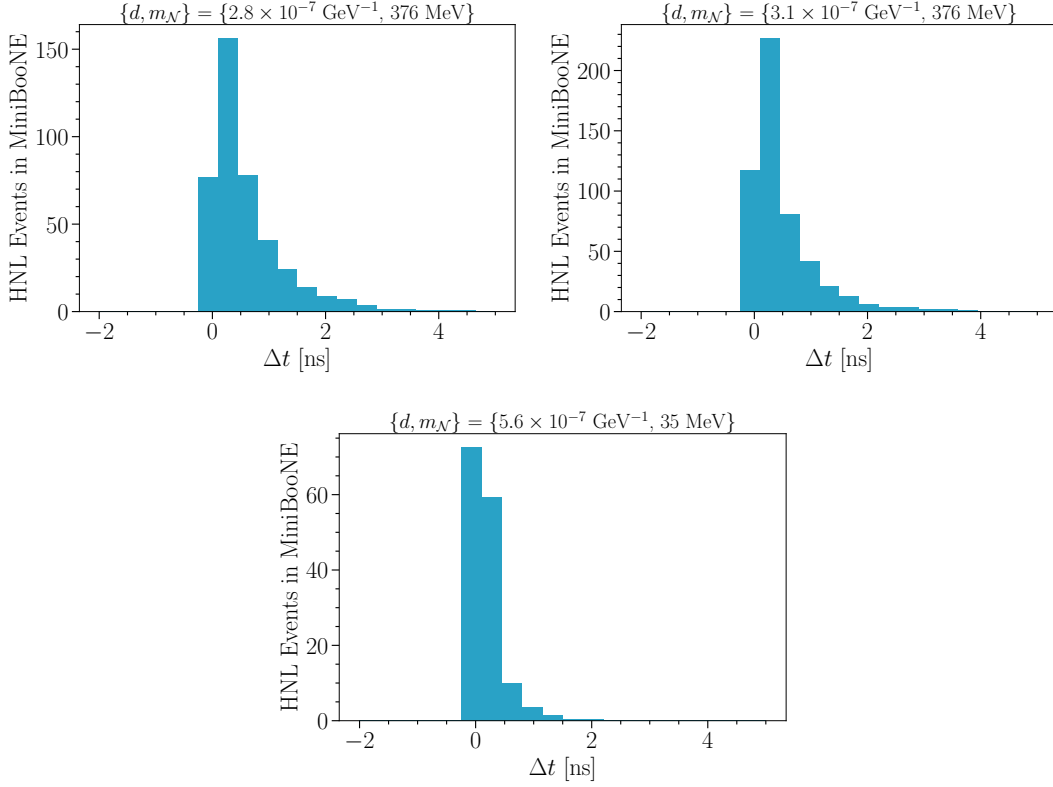
In reporting the tension, we make use of the probability associated with the Parameter Goodness of Fit Test, or PG Test, which is a standard in our field. In this test [6], the global (glob) set data is divided into disappearance (dis) and appearance (app) sets. One defines the χ^2 and degrees of freedom as:

$$\chi_{PG}^2 = \chi_{glob}^2 - (\chi_{app}^2 + \chi_{dis}^2), \quad (\text{A11})$$

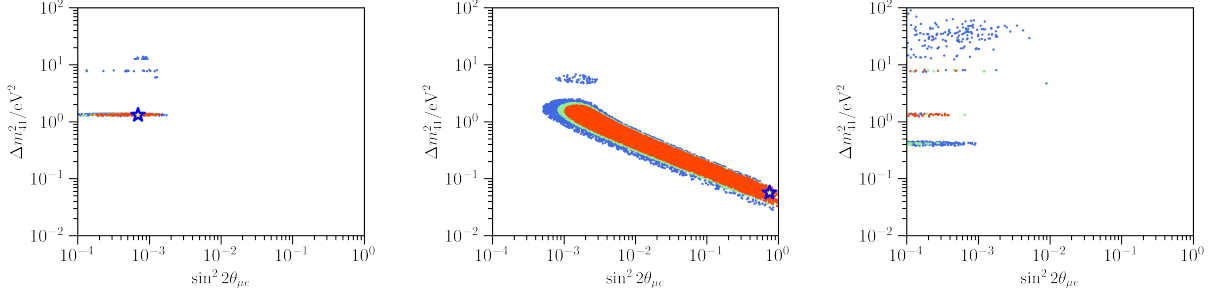
$$N_{PG} = (N_{app} + N_{dis}) - N_{glob}. \quad (\text{A12})$$

We quote the associated probability as the tension. Table III lists the inputs to the calculation that appears in this paper.

For the 3+1-only fit used in this article, we run the oscillation fit on the experiments that would not be sensitive



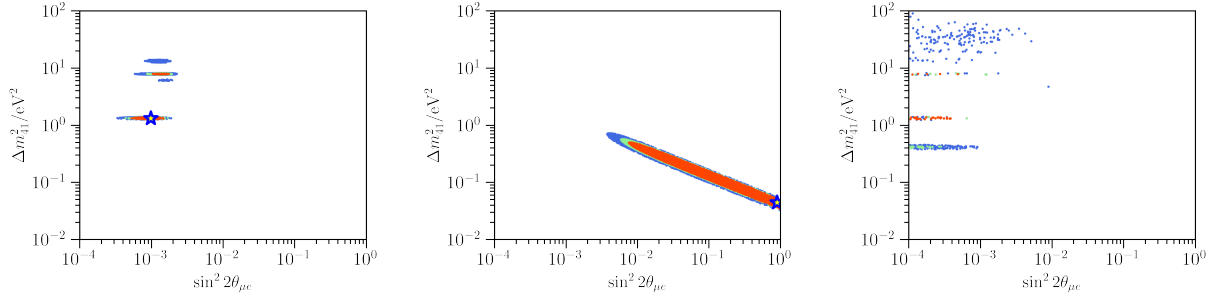
SUPPL. FIG. 4. Timing delay distributions for HNL events in the MiniBooNE detector, as defined in the text. The specific d and $m_{\mathcal{N}}$ values shown here come from Table II. Three different eV -scale oscillation amplitudes are considered: $\sin^2 2\theta = 6.9 \times 10^{-4}$ (top left), $\sin^2 2\theta = 3 \times 10^{-4}$ (top right), and $\sin^2 2\theta = 2 \times 10^{-3}$ (bottom).



SUPPL. FIG. 5. These plots show the best fit regions for the 3+1+only oscillation data sets used in this Letter. The left plot shows the best fit regions of the global fits, with 90%, 95%, and 99% regions shown in red, green, and blue, respectively. The middle plot shows the best fit region when only fitting to the appearance subset of data, while the right plot shows the best fit region when only fitting to the disappearance subset. The tension within this data set can be qualitatively seen by the fact that the best fit regions do not overlap between the appearance-only and disappearance-only data sets.

to the \mathcal{N} decay. As stated earlier, this procedure finds a best fit point of $\Delta m^2 = 1.32 \text{ eV}^2$ and $\sin^2 2\theta_{e\mu} = 6.9 \times 10^{-4}$, with an allowed range $\sin^2 2\theta_{\mu e} \in [3 \times 10^{-4}, 2 \times 10^{-3}]$ at the 90% CL. The best-fit regions are shown on the leftmost plot in Fig 5. The tension within this fit is demonstrated by separately fitting the appearance and disappearance data sets, which are shown in the middle and right plot in 5, respectively. This tension is found to have a p-value of 7×10^{-3} , with the relevant parameters summarized in Table III.

For completeness, we also provide a global fit including *all* experiments listed in Table II. These results, which we'll



SUPPL. FIG. 6. These plots show the best fit regions for the 3+1+complete oscillation data sets. This serves as an update to the fits provided in [3], and are not used in the preceding analysis. The left plot shows the best fit regions of this complete global fit, with 90%, 95%, and 99% regions shown in red, green, and blue, respectively. The middle plot shows the best fit region for the appearance subset of data, while the right plot shows the best fit region for the disappearance subset. As seen before, the global sterile neutrino oscillation model suffers from substantial tension.

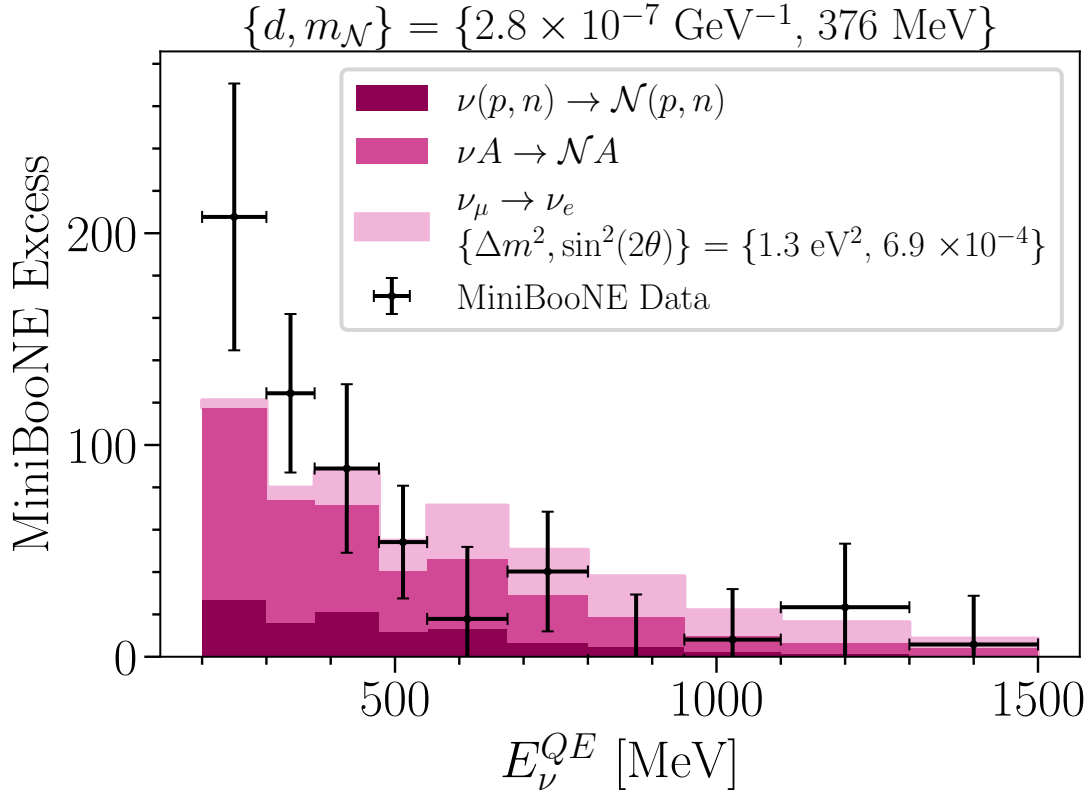
label “3+1-complete,” are not used in the preceding analysis. The best fit regions for this 3+1 global fit is shown in the left plot of Fig. 6, with the best fit point at $\sin^2(2\theta_{\mu e}) = 1 \times 10^{-3}$ and $\Delta m_{41}^2 = 1.32 \text{ eV}^2$. As has been seen before [1–4], this model suffers from a tension between the appearance and disappearance data sets. The best-fit regions of the appearance and disappearance data sets are shown in the middle and right plot of Fig. 6, respectively. The tension found in the global data set is found to have a p-value of 8×10^{-7} , with the relevant parameters summarized in Table III.

Our analysis fits to the MiniBooNE (BNB) neutrino energy distribution, which has been presented with statistical and systematic error. Specifically, the points and errors are taken from Fig. 19 of Ref. [70]. In this case, the data are the excess events when the MiniBooNE measurement is compared to the constrained backgrounds. It is important to note that for most neutrino energy bins, the systematic error dominates, and so is necessary to include in the uncertainty when performing the fit. The result of the $3 + 1 + \mathcal{N}$ energy fit has been shown in the paper in Fig. 3, left, and here we reproduce and enlarge the same figure in Fig. 7. Light pink indicates the oscillation component, with $\Delta m^2 = 1.3 \text{ eV}^2$ and $\sin^2 2\theta = 6.9 \times 10^{-4}$. The darker pink regions indicate the HNL decay component from both coherent and incoherent upscattering production, with $d = 2.8 \times 10^{-7} \text{ GeV}^{-1}$ and $m_{\mathcal{N}} = 376 \text{ MeV}$.

MiniBooNE has not provided a data release for the angular distribution of the electromagnetic shower in the

Experiment	Ref.	Type	In $3 + 1 + \mathcal{N}$ osc fit?	In $3 + 1 + \mathcal{N}$ decay fit?
Bugey	[39]	$\bar{\nu}_e \rightarrow \bar{\nu}_e$	Yes	No
NEOS	[40]	$\bar{\nu}_e \rightarrow \bar{\nu}_e$	Yes	No
DANSS	[41]	$\bar{\nu}_e \rightarrow \bar{\nu}_e$	Yes	No
PROSPECT	[42]	$\bar{\nu}_e \rightarrow \bar{\nu}_e$	Yes	No
STEREO	[43]	$\bar{\nu}_e \rightarrow \bar{\nu}_e$	Yes	No
KARMEN/LSND Cross Section	[44]	$\nu_e \rightarrow \nu_e$	Yes	No
Gallium	[45, 46]	$\nu_e \rightarrow \nu_e$	Yes	No
SciBooNE/MiniBooNE	[50]	$\bar{\nu}_\mu \rightarrow \bar{\nu}_\mu$	Yes	No
CCFR	[51]	$\bar{\nu}_\mu \rightarrow \bar{\nu}_\mu$	Yes	No
MINOS	[52, 53]	$\bar{\nu}_\mu \rightarrow \bar{\nu}_\mu$	Yes	No
SciBooNE/MiniBooNE	[54]	$\nu_\mu \rightarrow \nu_\mu$	Yes	No
CCFR	[51]	$\nu_\mu \rightarrow \nu_\mu$	Yes	No
CDHS	[55]	$\nu_\mu \rightarrow \nu_\mu$	Yes	No
MINOS	[56]	$\nu_\mu \rightarrow \nu_\mu$	Yes	No
LSND	[47]	$\bar{\nu}_\mu \rightarrow \bar{\nu}_e$	Yes	No
KARMEN	[48]	$\bar{\nu}_\mu \rightarrow \bar{\nu}_e$	Yes	No
MiniBooNE (BNB)	[58]	$\bar{\nu}_\mu \rightarrow \bar{\nu}_e$	No	No
NOMAD	[49]	$\nu_\mu \rightarrow \nu_e$	Yes	No
MiniBooNE (NuMI)	[59]	$\nu_\mu \rightarrow \nu_e$	No	No
MiniBooNE (BNB)	[70]	$\nu_\mu \rightarrow \nu_e$	No	Yes

SUPPL. TABLE II. Table of experimental results used in the fits in this paper.

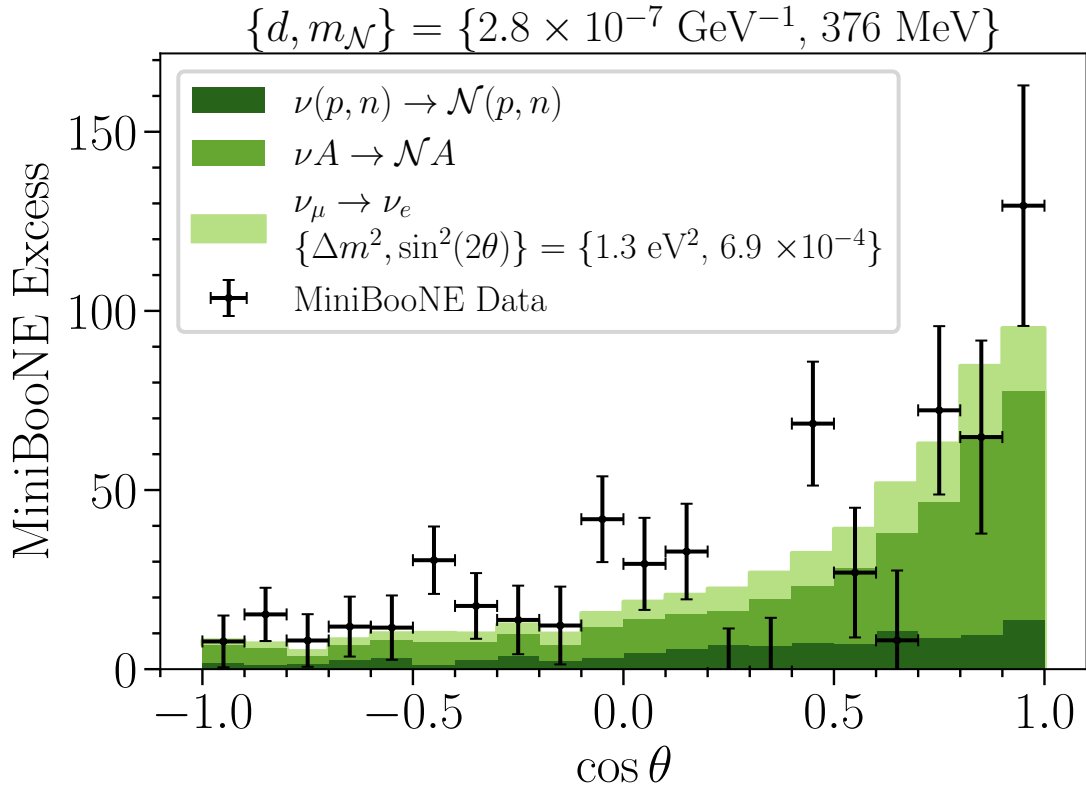


SUPPL. FIG. 7. Enlarged version of Fig. 3, left, in the paper. The prediction for the oscillation contribution to the $3+1+\mathcal{N}$ component is shown in light pink. The prediction for the \mathcal{N} decay component, from both coherent and incoherent upscattering, is shown in darker pink. See text in this appendix for explanation of the data.

Fit type:	3+1-only	3+1-complete
χ_{app}^2	48	79
N_{app}	2	2
χ_{dis}^2	557	557
N_{dis}	3	3
χ_{glob}^2	615	664
N_{glob}	3	3
χ_{PG}^2	10	28
N_{PG}	2	2
p -value	7E-03	8E-07
$N\sigma$	2.7σ	4.8σ

SUPPL. TABLE III. PG test results for 3+1 and our model, where Eqs. A11 and A12 explain how χ_{PG}^2 and N_{PG} are determined.

excess events. The data shown in Fig. 3, right, is obtained by subtracting the unconstrained backgrounds from the MiniBooNE measurement shown in Fig. 8 of Ref. [70]. Only statistical errors are provided by MiniBooNE at present. We note that one would expect the systematic uncertainty to be substantially larger, as was the case for the neutrino energy. Therefore, it would be interesting to repeat this analysis considering a robust treatment of the systematic errors in the angular distribution. Fig. 8 reproduces and enlarges Fig. 3, right, showing the oscillation component in light green and the HNL decay component from coherent/incoherent upscattering production in darker green. One can see that the oscillation component does not address the forward-peak in the MiniBooNE data while the decay component primarily addresses that peak.



SUPPL. FIG. 8. Enlarged version of Fig. 3, right, in the paper. The prediction for the oscillation contribution to the $3 + 1 + \mathcal{N}$ component is shown in light green. The prediction for the \mathcal{N} decay component, from both coherent and incoherent upscattering, is shown in darker green. See text in this appendix for explanation of the data.